Cross section and transverse single-spin asymmetry of η mesons in $p^{\uparrow} + p$ collisions at $\sqrt{s} = 200$ GeV at forward rapidity

A. Adare,[13] C. Aidala,[43,44] N.N. Ajitanand,[62] Y. Akiba,[56,57] R. Akimoto,[12] H. Al-Bataineh,[50] J. Alexander,[62] M. Alfred,[24] A. Angerami,[14] K. Aoki,[35,56] N. Apadula,[63] Y. Aramaki,[12,56] H. Asano,[35,56] E.T. Atomssa,[36,63] R. Averbeck,[63] T.C. Awes,[52] B. Azmoun,[7] V. Babintsev,[25] M. Bai,[6] G. Baksay,[19] L. Baksay,[19] N.S. Bandara,[43] B. Bannier,[63] K.N. Barish,[8] B. Bassalleck,[49] A.T. Basye,[1] S. Bathe,[5,8,57] V. Baublis,[55] C. Baumann,[45] A. Bazilevsky,[7] M. Beaumier,[8] S. Beckman,[13] S. Belikov,[7,*] R. Belmont,[44,67] R. Bennett,[63] A. Berdnikov,[59] Y. Berdnikov,[59] J.H. Bhom,[71] D. Black,[8] D.S. Blau,[34] J. Bok,[50] J.S. Bok,[71] K. Boyle,[57,63] M.L. Brooks,[39] J. Bryslawskyj,[5] H. Buesching,[7] V. Bumazhnov,[25] G. Bunce,[7,57] S. Butsyk,[39] S. Campbell,[29,63] A. Caringi,[46] C.-H. Chen,[57,63] C.Y. Chi,[14] M. Chiu,[7] I.J. Choi,[26,71] J.B. Choi,[10] R.K. Choudhury,[4] P. Christiansen,[41] T. Chujo,[66] P. Chung,[62] O. Chvala,[8] V. Cianciolo,[52] Z. Citron,[63,69] B.A. Cole,[14] Z. Conesa del Valle,[36] M. Connors,[63] M. Csanád,[17] T. Csörgő,[70] T. Dahms,[63] S. Dairaku,[35,56] I. Danchev,[67] K. Das,[20] A. Datta,[43,49] M.S. Daugherity,[1] G. David,[7] M.K. Dayananda,[21] K. DeBlasio,[49] K. Dehmelt,[63] A. Denisov,[25] A. Deshpande,[57,63] E.J. Desmond,[7] K.V. Dharmawardane,[50] O. Dietzsch,[60] L. Ding,[29] A. Dion,[29,63] J.H. Do,[71] M. Donadelli,[60] O. Drapier,[36] A. Drees,[63] K.A. Drees,[6] J.M. Durham,[39,63] A. Durum,[25] D. Dutta,[4] L. D'Orazio,[42] S. Edwards,[20] Y.V. Efremenko,[52] F. Ellinghaus,[13] T. Engelmore,[14] A. Enokizono,[52,56,58] H. En'yo,[56,57] S. Esumi,[66] K.O. Eyser,[7] B. Fadem,[46] N. Feege,[63] D.E. Fields,[49] M. Finger,[9] M. Finger, Jr.,[9] F. Fleuret,[36] S.L. Fokin,[34] Z. Fraenkel,[69,*] J.E. Frantz,[51,63] A. Franz,[7] A.D. Frawley,[20] K. Fujiwara,[56] Y. Fukao,[56] T. Fusayasu,[48] C. Gal,[63] P. Gallus,[15] P. Garg,[3] I. Garishvili,[64] H. Ge,[63] F. Giordano,[26] A. Glenn,[38] H. Gong,[63] M. Gonin,[36] Y. Goto,[56,57] R. Granier de Cassagnac,[36] N. Grau,[2,14] S.V. Greene,[67] G. Grim,[39] M. Grosse Perdekamp,[26] Y. Gu,[62] T. Gunji,[12] H. Guragain,[21] H.-Å. Gustafsson,[41,*] T. Hachiya,[56] J.S. Haggerty,[7] K.I. Hahn,[18] H. Hamagaki,[12] J. Hamblen,[64] R. Han,[54] S.Y. Han,[18] J. Hanks,[14,63] S. Hasegawa,[30] E. Haslum,[41] R. Hayano,[12] X. He,[21] M. Heffner,[38] T.K. Hemmick,[63] T. Hester,[8] J.C. Hill,[29] M. Hohlmann,[19] R.S. Hollis,[8] W. Holzmann,[14] K. Homma,[23] B. Hong,[33] T. Horaguchi,[23] D. Hornback,[64] T. Hoshino,[23] S. Huang,[67] T. Ichihara,[56,57] R. Ichimiya,[56] Y. Ikeda,[56,66] K. Imai,[30,35,56] Y. Imazu,[56] M. Inaba,[66] A. Iordanova,[8] D. Isenhower,[1] M. Ishihara,[56] M. Issah,[67] D. Ivanischev,[55] D. Ivanishchev,[55] Y. Iwanaga,[23] B.V. Jacak,[63] S.J. Jeon,[47] M. Jezghani,[21] J. Jia,[7,62] X. Jiang,[39] J. Jin,[14] B.M. Johnson,[7] T. Jones,[1] E. Joo,[33] K.S. Joo,[47] D. Jouan,[53] D.S. Jumper,[1,26] F. Kajihara,[12] J. Kamin,[63] J.H. Kang,[71] J.S. Kang,[22] J. Kapustinsky,[39] K. Karatsu,[35,56] M. Kasai,[56,58] D. Kawall,[43,57] M. Kawashima,[56,58] A.V. Kazantsev,[34] T. Kempel,[29] J.A. Key,[49] V. Khachatryan,[63] A. Khanzadeev,[55] K. Kihara,[66] K.M. Kijima,[23] J. Kikuchi,[68] A. Kim,[18] B.I. Kim,[33] C. Kim,[33] D.H. Kim,[18] D.J. Kim,[31] E.-J. Kim,[10] H.-J. Kim,[71] M. Kim,[61] Y.-J. Kim,[26] Y.K. Kim,[22] E. Kinney,[13] Á. Kiss,[17] E. Kistenev,[7] J. Klatsky,[20] D. Kleinjan,[8] P. Kline,[63] T. Koblesky,[13] L. Kochenda,[55] M. Kofarago,[17] B. Komkov,[55] M. Konno,[66] J. Koster,[26,57] D. Kotov,[55,59] A. Král,[15] A. Kravitz,[14] G.J. Kunde,[39] K. Kurita,[56,58] M. Kurosawa,[56,57] Y. Kwon,[71] G.S. Kyle,[50] R. Lacey,[62] Y.S. Lai,[14] J.G. Lajoie,[29] A. Lebedev,[29] D.M. Lee,[39] J. Lee,[18] K.B. Lee,[33,39] K.S. Lee,[33] S.H. Lee,[63] M.J. Leitch,[39] M.A.L. Leite,[60] M. Leitgab,[26] X. Li,[11] P. Lichtenwalner,[46] P. Liebing,[57] S.H. Lim,[71] L.A. Linden Levy,[13] T. Liška,[15] H. Liu,[39] M.X. Liu,[39] B. Love,[67] D. Lynch,[7] C.F. Maguire,[67] Y.I. Makdisi,[6] M. Makek,[69,72] M.D. Malik,[49] A. Manion,[63] V.I. Manko,[34] E. Mannel,[7,14] Y. Mao,[54,56] H. Masui,[66] F. Matathias,[14] M. McCumber,[39,63] P.L. McGaughey,[39] D. McGlinchey,[13,20] C. McKinney,[26] N. Means,[63] A. Meles,[50] M. Mendoza,[8] B. Meredith,[14,26] Y. Miake,[66] T. Mibe,[32] A.C. Mignerey,[42] K. Miki,[56,66] A.J. Miller,[1] A. Milov,[7,69] D.K. Mishra,[4] J.T. Mitchell,[7] S. Miyasaka,[56,65] S. Mizuno,[56,66] A.K. Mohanty,[4] P. Montuenga,[26] H.J. Moon,[47] T. Moon,[71] Y. Morino,[12] A. Morreale,[8] D.P. Morrison,[7,†] T.V. Moukhanova,[34] T. Murakami,[35,56] J. Murata,[56,58] A. Mwai,[62] S. Nagamiya,[32,56] J.L. Nagle,[13,‡] M. Naglis,[69] M.I. Nagy,[17,70] I. Nakagawa,[56,57] H. Nakagomi,[56,66] Y. Nakamiya,[23] K.R. Nakamura,[35,56] T. Nakamura,[56] K. Nakano,[56,65] S. Nam,[18] C. Nattrass,[64] P.K. Netrakanti,[4] J. Newby,[38] M. Nguyen,[63] M. Nihashi,[23,56] T. Niida,[66] R. Nouicer,[7,57] N. Novitzky,[31] A.S. Nyanin,[34] C. Oakley,[21] E. O'Brien,[7] S.X. Oda,[12] C.A. Ogilvie,[29] M. Oka,[66] K. Okada,[57] Y. Onuki,[56] J.D. Orjuela Koop,[13] A. Oskarsson,[41] M. Ouchida,[23,56] H. Ozaki,[66] K. Ozawa,[12,32] R. Pak,[7] V. Pantuev,[27,63] V. Papavassiliou,[50] I.H. Park,[18] S. Park,[61] S.K. Park,[33] W.J. Park,[33] S.F. Pate,[50] L. Patel,[21] M. Patel,[29] H. Pei,[29] J.-C. Peng,[26] H. Pereira,[16] D.V. Perepelitsa,[7,14] G.D.N. Perera,[50] D.Yu. Peressounko,[34] J. Perry,[29] R. Petti,[63] C. Pinkenburg,[7] R. Pinson,[1] R.P. Pisani,[7] M. Proissl,[63] M.L. Purschke,[7] H. Qu,[21] J. Rak,[31] I. Ravinovich,[69] K.F. Read,[52,64] S. Rembeczki,[19] K. Reygers,[45] D. Reynolds,[62] V. Riabov,[55] Y. Riabov,[55,59] E. Richardson,[42] N. Riveli,[51] D. Roach,[67] G. Roche,[40] S.D. Rolnick,[8] M. Rosati,[29] C.A. Rosen,[13] S.S.E. Rosendahl,[41] Z. Rowan,[5] J.G. Rubin,[44] P. Ružička,[28] B. Sahlmueller,[45,63] N. Saito,[32] T. Sakaguchi,[7] K. Sakashita,[56,65] H. Sako,[30] V. Samsonov,[55] S. Sano,[12,68] M. Sarsour,[21] S. Sato,[30] T. Sato,[66] S. Sawada,[32] B. Schaefer,[67] B.K. Schmoll,[64]

K. Sedgwick,[8] J. Seele,[13,57] R. Seidl,[26,56,57] A. Sen,[64] R. Seto,[8] P. Sett,[4] A. Sexton,[42] D. Sharma,[63,69] I. Shein,[25] T.-A. Shibata,[56,65] K. Shigaki,[23] M. Shimomura,[29,66] K. Shoji,[35,56] P. Shukla,[4] A. Sickles,[7] C.L. Silva,[29,39] D. Silvermyr,[52] C. Silvestre,[16] K.S. Sim,[33] B.K. Singh,[3] C.P. Singh,[3] V. Singh,[3] M. Slunečka,[9] R.A. Soltz,[38] W.E. Sondheim,[39] S.P. Sorensen,[64] I.V. Sourikova,[7] P.W. Stankus,[52] E. Stenlund,[41] M. Stepanov,[43] S.P. Stoll,[7] T. Sugitate,[23] A. Sukhanov,[7] T. Sumita,[56] J. Sun,[63] J. Sziklai,[70] E.M. Takagui,[60] A. Takahara,[12] A. Taketani,[56,57] R. Tanabe,[66] Y. Tanaka,[48] S. Taneja,[63] K. Tanida,[35,56,57,61] M.J. Tannenbaum,[7] S. Tarafdar,[3,69] A. Taranenko,[62] H. Themann,[63] D. Thomas,[1] T.L. Thomas,[49] A. Timilsina,[29] T. Todoroki,[56,66] M. Togawa,[57] A. Toia,[63] L. Tomášek,[28] M. Tomášek,[15] H. Torii,[23,56] M. Towell,[1] R. Towell,[1] R.S. Towell,[1] I. Tserruya,[69] Y. Tsuchimoto,[23] C. Vale,[7] H. Valle,[67] H.W. van Hecke,[39] M. Vargyas,[70] E. Vazquez-Zambrano,[14] A. Veicht,[26] J. Velkovska,[67] R. Vértesi,[70] M. Virius,[15] V. Vrba,[15,28] E. Vznuzdaev,[55] X.R. Wang,[50] D. Watanabe,[23] K. Watanabe,[66] Y. Watanabe,[56,57] Y.S. Watanabe,[32] F. Wei,[29,50] R. Wei,[62] J. Wessels,[45] S. Whitaker,[29] S.N. White,[7] D. Winter,[14] S. Wolin,[26] C.L. Woody,[7] R.M. Wright,[1] M. Wysocki,[13,52] B. Xia,[51] L. Xue,[21] S. Yalcin,[63] Y.L. Yamaguchi,[12,56] K. Yamaura,[23] R. Yang,[26] A. Yanovich,[25] J. Ying,[21] S. Yokkaichi,[56,57] I. Yoon,[61] Z. You,[54] G.R. Young,[52] I. Younus,[37,49] I.E. Yushmanov,[34] W.A. Zajc,[14] A. Zelenski,[6] and S. Zhou[11]

(PHENIX Collaboration)

[1]*Abilene Christian University, Abilene, Texas 79699, USA*
[2]*Department of Physics, Augustana College, Sioux Falls, South Dakota 57197, USA*
[3]*Department of Physics, Banaras Hindu University, Varanasi 221005, India*
[4]*Bhabha Atomic Research Centre, Bombay 400 085, India*
[5]*Baruch College, City University of New York, New York, New York, 10010 USA*
[6]*Collider-Accelerator Department, Brookhaven National Laboratory, Upton, New York 11973-5000, USA*
[7]*Physics Department, Brookhaven National Laboratory, Upton, New York 11973-5000, USA*
[8]*University of California - Riverside, Riverside, California 92521, USA*
[9]*Charles University, Ovocný trh 5, Praha 1, 116 36, Prague, Czech Republic*
[10]*Chonbuk National University, Jeonju, 561-756, Korea*
[11]*Science and Technology on Nuclear Data Laboratory, China Institute of Atomic Energy, Beijing 102413, People's Republic of China*
[12]*Center for Nuclear Study, Graduate School of Science, University of Tokyo, 7-3-1 Hongo, Bunkyo, Tokyo 113-0033, Japan*
[13]*University of Colorado, Boulder, Colorado 80309, USA*
[14]*Columbia University, New York, New York 10027 and Nevis Laboratories, Irvington, New York 10533, USA*
[15]*Czech Technical University, Zikova 4, 166 36 Prague 6, Czech Republic*
[16]*Dapnia, CEA Saclay, F-91191, Gif-sur-Yvette, France*
[17]*ELTE, Eötvös Loránd University, H - 1117 Budapest, Pázmany Péter sétány 1/A, Hungary*
[18]*Ewha Womans University, Seoul 120-750, Korea*
[19]*Florida Institute of Technology, Melbourne, Florida 32901, USA*
[20]*Florida State University, Tallahassee, Florida 32306, USA*
[21]*Georgia State University, Atlanta, Georgia 30303, USA*
[22]*Hanyang University, Seoul 133-792, Korea*
[23]*Hiroshima University, Kagamiyama, Higashi-Hiroshima 739-8526, Japan*
[24]*Department of Physics and Astronomy, Howard University, Washington, DC 20059, USA*
[25]*IHEP Protvino, State Research Center of Russian Federation, Institute for High Energy Physics, Protvino, 142281, Russia*
[26]*University of Illinois at Urbana-Champaign, Urbana, Illinois 61801, USA*
[27]*Institute for Nuclear Research of the Russian Academy of Sciences, prospekt 60-letiya Oktyabrya 7a, Moscow 117312, Russia*
[28]*Institute of Physics, Academy of Sciences of the Czech Republic, Na Slovance 2, 182 21 Prague 8, Czech Republic*
[29]*Iowa State University, Ames, Iowa 50011, USA*
[30]*Advanced Science Research Center, Japan Atomic Energy Agency, 2-4 Shirakata Shirane, Tokai-mura, Naka-gun, Ibaraki-ken 319-1195, Japan*
[31]*Helsinki Institute of Physics and University of Jyväskylä, P.O.Box 35, FI-40014 Jyväskylä, Finland*
[32]*KEK, High Energy Accelerator Research Organization, Tsukuba, Ibaraki 305-0801, Japan*
[33]*Korea University, Seoul, 136-701, Korea*
[34]*Russian Research Center "Kurchatov Institute," Moscow, 123098 Russia*
[35]*Kyoto University, Kyoto 606-8502, Japan*
[36]*Laboratoire Leprince-Ringuet, Ecole Polytechnique, CNRS-IN2P3, Route de Saclay, F-91128, Palaiseau, France*
[37]*Physics Department, Lahore University of Management Sciences, Lahore 54792, Pakistan*
[38]*Lawrence Livermore National Laboratory, Livermore, California 94550, USA*
[39]*Los Alamos National Laboratory, Los Alamos, New Mexico 87545, USA*
[40]*LPC, Université Blaise Pascal, CNRS-IN2P3, Clermont-Fd, 63177 Aubiere Cedex, France*
[41]*Department of Physics, Lund University, Box 118, SE-221 00 Lund, Sweden*
[42]*University of Maryland, College Park, Maryland 20742, USA*
[43]*Department of Physics, University of Massachusetts, Amherst, Massachusetts 01003-9337, USA*

[44]Department of Physics, University of Michigan, Ann Arbor, Michigan 48109-1040, USA
[45]Institut fur Kernphysik, University of Muenster, D-48149 Muenster, Germany
[46]Muhlenberg College, Allentown, Pennsylvania 18104-5586, USA
[47]Myongji University, Yongin, Kyonggido 449-728, Korea
[48]Nagasaki Institute of Applied Science, Nagasaki-shi, Nagasaki 851-0193, Japan
[49]University of New Mexico, Albuquerque, New Mexico 87131, USA
[50]New Mexico State University, Las Cruces, New Mexico 88003, USA
[51]Department of Physics and Astronomy, Ohio University, Athens, Ohio 45701, USA
[52]Oak Ridge National Laboratory, Oak Ridge, Tennessee 37831, USA
[53]IPN-Orsay, Universite Paris Sud, CNRS-IN2P3, BP1, F-91406, Orsay, France
[54]Peking University, Beijing 100871, People's Republic of China
[55]PNPI, Petersburg Nuclear Physics Institute, Gatchina, Leningrad Region, 188300, Russia
[56]RIKEN Nishina Center for Accelerator-Based Science, Wako, Saitama 351-0198, Japan
[57]RIKEN BNL Research Center, Brookhaven National Laboratory, Upton, New York 11973-5000, USA
[58]Physics Department, Rikkyo University, 3-34-1 Nishi-Ikebukuro, Toshima, Tokyo 171-8501, Japan
[59]Saint Petersburg State Polytechnic University, St. Petersburg, 195251 Russia
[60]Universidade de São Paulo, Instituto de Física, Caixa Postal 66318, São Paulo CEP05315-970, Brazil
[61]Department of Physics and Astronomy, Seoul National University, Seoul 151-742, Korea
[62]Chemistry Department, Stony Brook University, SUNY, Stony Brook, New York 11794-3400, USA
[63]Department of Physics and Astronomy, Stony Brook University, SUNY, Stony Brook, New York 11794-3800, USA
[64]University of Tennessee, Knoxville, Tennessee 37996, USA
[65]Department of Physics, Tokyo Institute of Technology, Oh-okayama, Meguro, Tokyo 152-8551, Japan
[66]Institute of Physics, University of Tsukuba, Tsukuba, Ibaraki 305, Japan
[67]Vanderbilt University, Nashville, Tennessee 37235, USA
[68]Waseda University, Advanced Research Institute for Science and Engineering, 17 Kikui-cho, Shinjuku-ku, Tokyo 162-0044, Japan
[69]Weizmann Institute, Rehovot 76100, Israel
[70]Institute for Particle and Nuclear Physics, Wigner Research Centre for Physics, Hungarian Academy of Sciences (Wigner RCP, RMKI) H-1525 Budapest 114, POBox 49, Budapest, Hungary
[71]Yonsei University, IPAP, Seoul 120-749, Korea
[72]University of Zagreb, Faculty of Science, Department of Physics, Bijenička 32, HR-10002 Zagreb, Croatia

(Dated: June 16, 2014)

We present a measurement of the cross section and transverse single-spin asymmetry (A_N) for η mesons at large pseudorapidity from $\sqrt{s} = 200$ GeV $p^{\uparrow} + p$ collisions. The measured cross section for $0.5 < p_T < 5.0$ GeV/c and $3.0 < |\eta| < 3.8$ is well described by a next-to-leading-order perturbative-quantum-chromodynamics calculation. The asymmetries A_N have been measured as a function of Feynman-x (x_F) from $0.2 < |x_F| < 0.7$, as well as transverse momentum (p_T) from $1.0 < p_T < 4.5$ GeV/c. The asymmetry averaged over positive x_F is $\langle A_N \rangle = 0.061 \pm 0.014$. The results are consistent with prior transverse single-spin measurements of forward η and π^0 mesons at various energies in overlapping x_F ranges. Comparison of different particle species can help to determine the origin of the large observed asymmetries in $p^{\uparrow} + p$ collisions.

PACS numbers: 25.75.Dw

I. INTRODUCTION

Since the proton's magnetic moment was revealed to be 2.79 times the size of the Dirac magnetic moment [1], studying the internal structure of the proton has been a vibrant field of physics research. Early deep-inelastic electron-nucleon scattering (DIS) experiments found that leptons were elastically scattered off of partons [2–4], and further measurements have led to detailed understanding of the parton distribution functions (PDFs) that can be used to describe the collinear quark and gluon structure of the nucleon. At leading order in a perturbative quantum chromodynamics (pQCD) expansion in the strong coupling α_s, PDF $f(x)$ represents the probability of a parton of flavor f carrying momentum fraction x of the total proton momentum. The PDFs themselves are nonperturbative and cannot be calculated directly in pQCD; they must instead be extracted from experimental measurements. From the development of QCD until the 1990s, experimental and theoretical studies focused on the one-dimensional momentum structure of the nucleon, in which the partons are treated as moving collinearly with the parent nucleon. Over the last two decades, a variety of theoretical and experimental tools have been developed to study other aspects of nucleon structure, including parton transverse dynamics within the nucleon. The measurement of transverse single spin asymmetries (SSAs) provides one window into dynamical

*Deceased
†PHENIX Co-Spokesperson: morrison@bnl.gov
‡PHENIX Co-Spokesperson: jamie.nagle@colorado.edu

spin-momentum correlations both in QCD bound states and in the process of partonic hadronization.

Leading-twist pQCD calculations predict very small transverse single spin asymmetries, less than $\mathcal{O}(10^{-4})$ at high-p_T ($p_T >$ few GeV/c) [5]. However, strikingly large transverse SSAs, up to $\sim 40\%$, have been measured at forward rapidity for hadrons produced from transversely polarized proton collisions ($p^{\uparrow} + p \rightarrow h + X$), revealing significant spin-momentum correlations in the non-perturbative structure of the proton. These asymmetries have been observed for collision energies ranging from $\sqrt{s} = 4.9$ to 500 GeV [6–16] and for hadron transverse momenta (p_T) up to 7 GeV/c [16]. The persistence of transverse SSAs into kinematic regimes where pQCD is applicable offers an opportunity to describe this non-perturbative behavior in terms of well-defined functions using the framework of pQCD. At midrapidity, no significant A_N has been observed [15, 17].

Multiple approaches have been proposed to describe the large transverse SSAs observed in hadronic reactions. Transverse-momentum-dependent (TMD) PDFs include explicit dependence not only on the partonic collinear momentum fraction but also on the partonic transverse momentum (k_T) within the nucleon. Similarly, TMD fragmentation functions (FFs) depend on both the collinear momentum fraction of the scattered parton acquired by the produced hadron as well as the transverse momentum of the hadron with respect to the direction of the scattered parton. Reactions involving scattering of a proton with its spin perpendicular to its momentum inducing the production of a hadron can provide sensitivity to both initial-state (PDF) and final-state (FF) effects.

Sivers proposed a TMD PDF [18, 19] as a possible origin of the large observed transverse SSAs, corresponding to a correlation between the spin of the proton and the transverse momentum of the quarks. Semi-inclusive DIS experiments have found evidence for a nonzero Sivers TMD PDF [20–23]. Collins alternatively proposed a TMD FF [24] that generates transverse SSAs, corresponding to a correlation between the (transverse) polarization of a scattered quark and the angular distribution of pions in the quark jet. The outgoing quarks in $p^{\uparrow}$+p collisions will have a net transverse polarization if the transversity distribution in the proton is nonzero. Electron-positron annihilation, as well as semi-inclusive DIS measurements, have now found evidence for a nonzero Collins TMD FF as well as a nonzero transversity distribution [20, 22, 25–29]. All these results indicate that there are sizable spin-momentum correlation effects in QCD bound states as well as in the process of hadronization.

While these spin-momentum correlations are present in the proton and in the process of hadronization, inclusive hadron production in $p^{\uparrow}$+p collisions cannot probe TMD PDFs and FFs directly as a function of k_T. However, these asymmetries do have sensitivity to the TMD PDFs and FFs integrated over k_T, and attempts to describe the data phenomenologically using the Sivers and Collins effects have been done [30–32].

Perturbative QCD calculations using collinear higher-twist quark-gluon correlations [33–37] can be performed and compared to data for inclusive SSAs in hadronic collisions. While these correlation functions do not contain direct information on the transverse momentum distributions of partons, this approach has been related to k_T-moments of TMD PDFs and FFs such as the Sivers and Collins functions for multiparton correlations in the initial and final state, respectively [38]. Prior RHIC transverse SSA measurements for inclusive hadron production have been described relatively well by a combination of twist-3 effects in the initial and final states [39–42], but further refinement in both the theoretical calculations, for example through a better understanding of uncertainties, and in experimental measurements, for example through multi-differential measurements in more than one kinematic variable simultaneously, will be needed to test and understand these correlations in detail.

It has been predicted that TMD-factorization may be broken when the partonic transverse momentum is explicitly taken into account, and the partons in the two incoming protons can no longer be described by independent PDFs but instead become correlated across the two protons [43]. In this case any phenomenology used to describe the asymmetries might become more complex, depending on the size of the effects from factorization breaking. The breakdown of TMD-factorization leads to the prediction of additional spin asymmetries in the case of hadron production in $p^{\uparrow}$+p collisions [44], with the possible magnitude of any new asymmetries still unknown. These effects, due to color exchange, will be interesting to explore further at RHIC once phenomenological predictions become available.

This paper reports on measurements of the cross section and transverse single spin asymmetry for η mesons at forward pseudorapidity ($3.0 < |\eta| < 3.8$) from the 2008 RHIC data taking period at $\sqrt{s} = 200$ GeV. A total integrated luminosity of $\mathcal{L} = 6.65$ pb^{-1} was sampled for these results. The measurement of different produced particle species will help to advance our understanding of the transverse SSAs (A_N) observed in $p^{\uparrow}$+p collisions. The comparison of pions, η mesons, and kaons can shed light on initial- versus final-state spin-momentum correlations as well as possible isospin, strangeness, and mass effects.

A review of the RHIC polarized p+p collider facility and the PHENIX experiment and detectors used for the measurements is given (Section II), followed by a description of the analysis procedure (Section III) used to procure the measurements of the cross section (Section IV) and transverse single spin asymmetry (Section V). A final section is reserved for discussion of the results derived from these measurements.

II. EXPERIMENT

A. RHIC polarized p+p collider

The Relativistic Heavy Ion Collider (RHIC) is a particle accelerator located at Brookhaven National Laboratory. RHIC has the capability of bunching, storing, accelerating, and colliding polarized protons [45], as well as other ions, over a broad range of center-of-mass energies ($\sqrt{s} = 62.4$ to 510 GeV for polarized protons). The injected beam into RHIC is typically made up of 111 bunches of polarized protons, which contain up to $\mathcal{O}(10^{11})$ protons per bunch for p+p collisions and are collided at several different points around the ring. One such interaction point is located at the PHENIX experiment [46]. For the 2008 RHIC p+p running, PHENIX (Fig. 1) consisted of two Spectrometer arms at central pseudorapidity $|\eta| < 0.35$, two Muon arms at pseudorapidity $1.2 < |\eta| < 2.4$, two global detectors, and two calorimeters (called the MPC detector) at forward pseudorapidity $3.1 < |\eta| < 3.9$.

A key aspect of the asymmetry measurements is the ability to align the spin vectors of the protons in the beam in a desired direction. The net fraction of protons in the beam with their spin vectors aligned along this desired direction is called the polarization (P). This must be measured to provide the correct scale for any asymmetry measurement. The polarization of the beams in RHIC is determined to within an uncertainty $\Delta P/P \sim 4\%$ using two different kinds of polarimeters: a Proton-Carbon polarimeter [47] and a Hydrogen-Jet polarimeter [48]. The Proton-Carbon polarimeter provides fast relative measurements of the polarization several times during a fill, while the Hydrogen-Jet polarimeter measurement takes several hours but yields the absolute polarization.

The polarization direction alternates for consecutive bunches which minimizes potential time-dependent and spin-dependent systematic uncertainties. In particular, detector efficiency and acceptance effects are minimized, as spin direction alternation in bunches allows use of the same detector for both polarization directions. During the 2008 RHIC run, the average clockwise beam (also known as the blue-beam) polarization was measured to be $P = 0.490 \pm 0.017$, while the average counter-clockwise beam (yellow) polarization was $P = 0.410 \pm 0.015$. The stable polarization direction in RHIC is transverse, *i.e.*, perpendicular to the accelerator plane.

B. PHENIX Local Polarimetry

The polarization direction is also measured locally at PHENIX using a pair of Zero-Degree Calorimeters (ZDCs). The ZDCs comprise two hadronic calorimeters, located ± 18 m from the nominal PHENIX interaction point. A shower maximum detector (SMD) combined with the ZDC measures the transverse single spin asymmetry of very forward ($\eta \gtrsim 6$) neutrons which is found to be nonzero, and as large as $A_N \sim 10\%$ [49, 50]. A study of neutron A_N in 2008 using the ZDC/SMD showed that the North-going (blue) polarization axis was oriented off-vertical by $\phi_{blue} = 0.263 \pm 0.03\,(\text{stat}) \pm 0.090\,(\text{syst})$ radians. The South-going polarization axis was found to be consistent with the nominal vertical direction, $\phi_{yellow} = 0.019 \pm 0.048\,(\text{stat}) \pm 0.103\,(\text{syst})$.

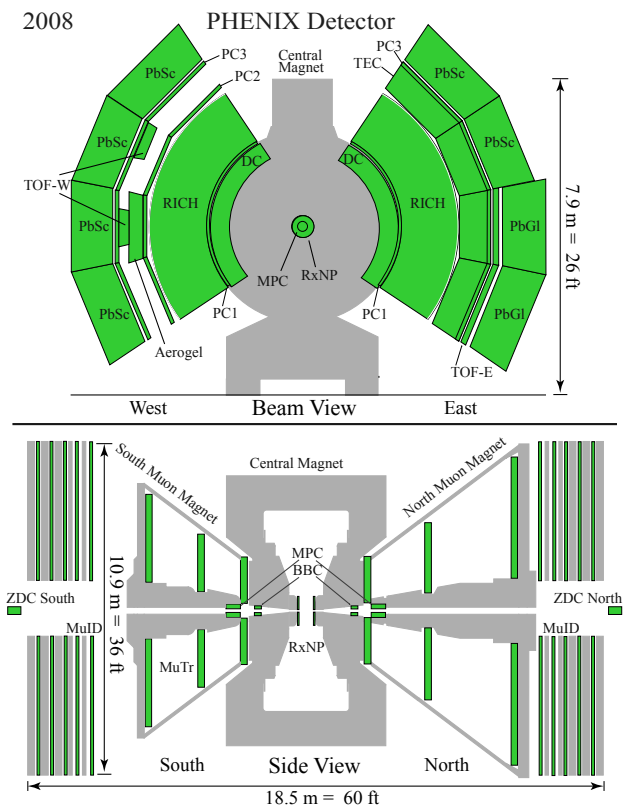

FIG. 1: The PHENIX detector configuration during the 2008 RHIC run.

C. PHENIX Beam-Beam Counters

The Beam-Beam Counters (BBC), see Fig. 1, comprise two arrays of 64 quartz Čerenkov radiators connected to photomultiplier tubes (PMTs). The BBC is $z = \pm 144$ cm from the nominal interaction point and covers $3.0 < |\eta| < 3.9$. The primary functions of this detector are to measure the position of the collision along the beam (z) axis to a precision of $\sigma(z_{vertex}) = 2$ cm, to provide a minimally biased trigger, and to measure the luminosity.

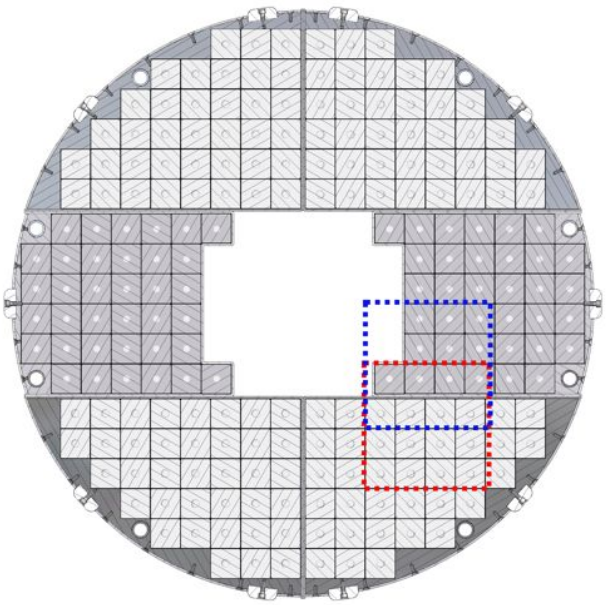

FIG. 2: (Color Online) A schematic of the North MPC as it appears in PHENIX. The right side shows the bare towers, *i.e.* without Front End Electronics. The red and blue squares drawn on the MPC demonstrate an example of two overlapping 4×4 trigger tiles.

D. PHENIX MPC detector

The Muon Piston Calorimeter (MPC) comprises two forward electromagnetic calorimeters, referred to as the South and North MPC, see Fig. 1, placed ±220 cm from the nominal interaction point along the beam axis. The South (North) MPC is made up of 196 (220) $2.2 \times 2.2 \times 18\,\mathrm{cm}^3$ $PbWO_4$ crystal towers, and is read out with Hamamatsu S8664-55 avalanche photo-diodes (APD). The MPC covers the pseudorapidity regions -3.7 $< \eta <$ -3.1 and $3.1 < \eta < 3.9$, respectively. The primary goal of the MPC is to identify π^0 and η mesons and measure their energy.

$PbWO_4$ crystals were chosen for their short radiation length (0.89 cm) and small Molière radius (2.0 cm). Similar $PbWO_4$ crystals were originally used and extensively tested for the PHOS detector [51], part of the ALICE experiment at CERN. The MPC is not cooled, and runs at the ambient temperature of its location in PHENIX. The gain variation with time, due largely to temperature variations and radiation damage to the crystals and APDs, is tracked using a LED calibration system. The absolute gain calibration comprises the LED tracking and tower by tower calibrations using π^0s. The relative energy resolution after calibration was found to be $\sigma(E)/E = 13\%/\sqrt{E} \oplus 8\%$. Comparisons between the π^0 and η-meson using real data and simulations showed that an overall energy scale uncertainty of 2% remained after all the calibrations, and also determined that the position resolution for clusters was about 2 mm. A schematic of the North MPC is given in Fig. 2.

E. Triggers

Readout of the PHENIX detector was done using one of two independent triggers for this analysis. The minimum bias (MB) trigger initiated readout when at least one BBC PMT in each array is hit, and when the collision vertex is within $|z| < 30$ cm of the nominal interaction point in PHENIX. As the number of collisions delivered by RHIC exceeds the data-taking rate of the PHENIX data acquisition system, only a small fraction of events can be recorded with "minimum bias." To enhance the more rare (higher momentum) η mesons in the data stream an additional trigger is used to record the high-p_T part of the cross section. This higher momentum trigger (called the 4×4B trigger) records an event when the total sum in any of the 4×4 trigger arrays of MPC towers satisfies an energy threshold of $E \gtrsim 20$ GeV. The 4×4 trigger arrays are particular groupings of towers and are called *tiles*. Each tile overlaps by 2 towers in the horizontal and vertical directions, as shown in Fig. 2, to provide even coverage for the trigger over the whole detector. The 4×4B trigger is formed without the requirement of a collision vertex from the BBCs.

III. IDENTIFICATION OF η MESONS IN THE MPC

To identify η mesons in the MPC, the decay channel $\eta \rightarrow \gamma\gamma$ is used which has a branching ratio of $BR = 0.3941 \pm 0.0020$ [52]. Clusters of MPC towers from a single event are combined to form photon candidates. To increase the likelihood that a cluster is due to a real photon, clusters which do not possess the characteristic electromagnetic shower shape are discarded. Clusters with their central tower tagged as noisy or inactive are also removed from the analysis. Once a sample of clusters is reduced to an enhanced sample of real photon candidates, clusters are paired together and an invariant mass is calculated, Eq. 1:

$$M_{\gamma\gamma} = \sqrt{4 \cdot E_1 \cdot E_2} \cdot \sin(\theta_{12}/2) \qquad (1)$$

where $E_{1,2}$ is the measured energy of each cluster, and θ_{12} is the opening angle between the momentum vectors of the two clusters. Additional kinematic cuts are made on paired clusters for the minimum bias and 4×4B data sets. A minimum energy $E_1 + E_2 > 7$ GeV and 10 GeV respectively is imposed. A maximum energy asymmetry, $\alpha = |\frac{E_1 - E_2}{E_1 + E_2}|$, of $\alpha = 0.6$ and 0.8, respectively, is required. The difference in the energy asymmetry cut between the two triggers is due to differences in the signal to background figure of merit. Finally, the separation between the two clusters ΔR has to be greater than 2.6 cm, minimizing merging effects between cluster showers. After

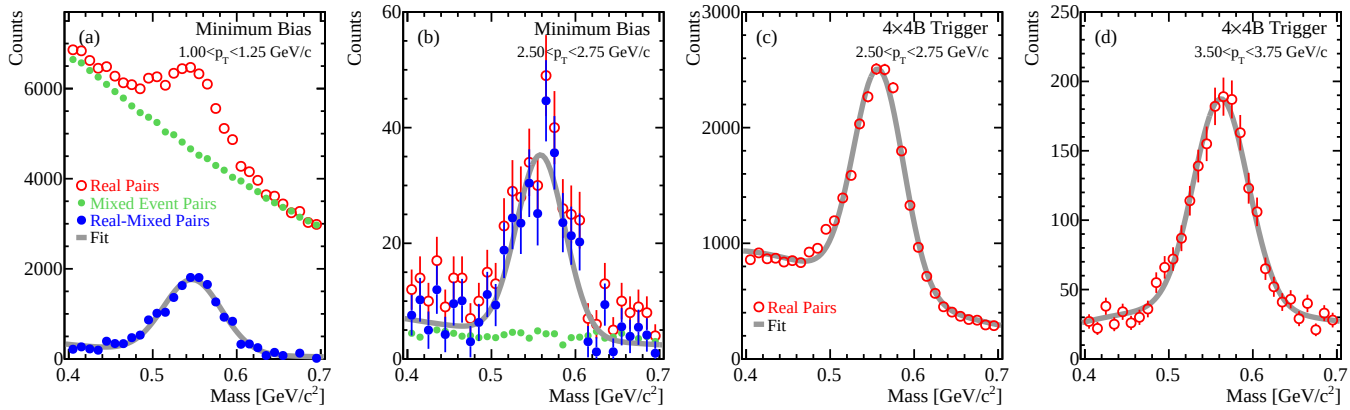

FIG. 3: (Color online) The invariant mass distribution for minimum bias (panels (a) and (b)) and 4×4B (panels (c) and (d)) samples. In all panels, open red circles represent all real pairs formed from MPC clusters. In panels (a) and (b) the small green closed symbols show the combinatorial background from mixed events (see text) and the closed blue symbols show the combinatorial-subtracted real pairs. Panels (b) and (c) show the same p_T selection and illustrate the importance of triggering to enhance the statistical significance at large momenta. Grey lines show the fit to the data used to extract the yield.

the application of these cuts, the invariant mass is calculated for all pairs, which is shown in Fig. 3 as open symbols.

IV. THE η MESON CROSS SECTION

The cross section can be written in terms of measured quantities as:

$$E\frac{d^3\sigma_h}{dp^3} = \frac{1}{\mathcal{L}_{\rm pp,inel}}\frac{1}{2\pi p_T}\frac{\Delta N_\eta^{\rm meas}}{BR\cdot\epsilon_{\rm reco}\cdot\epsilon_{\rm trig}\Delta p_T\Delta y} \qquad (2)$$

where $\Delta N_\eta^{\rm meas}$ is the number of measured (raw) η mesons over a rapidity range Δy and transverse momentum interval Δp_T. Note $\Delta y \approx \Delta\eta$ for η mesons at forward rapidity at the p_T measured in this analysis. The data are scaled by the integrated luminosity ($\mathcal{L}_{\rm pp,inel}$) and the branching fraction, BR, for this decay channel. To account for inefficiency in triggering and reconstruction, the $\Delta N_\eta^{\rm meas}$ is corrected by factors $\epsilon_{\rm trig}$ and $\epsilon_{\rm reco}$ respectively. Each of these components is described in the following sections.

A. Integrated Luminosity ($\mathcal{L}_{\rm pp,inel}$)

The luminosity is calculated as the ratio of the number of minimum bias events sampled for each trigger condition, within $|z| < 30$cm, divided by the part of the p+p cross section to which the BBCs are sensitive. This cross section is $\sigma_{\rm pp}^{\rm BBC} = 23.0 \pm 2.3$ mb which is determined using a Vernier Scan procedure [53]. The total integrated luminosity of the minimum bias dataset is $\mathcal{L}_{\rm MB} = 0.0192\,{\rm pb}^{-1}$ and that of the 4×4B dataset is $\mathcal{L}_{4\times4\rm B} = 3.87\,{\rm pb}^{-1}$.

B. Yield extraction ($\Delta N_\eta^{\rm meas}$)

The invariant mass distribution (Fig. 3) has two distinct components: correlated pairs (for example from η meson decays) and uncorrelated (combinatorial) background pairs, due to pairing of clusters from different parent sources. To account for this combinatorial background in the minimum bias dataset ($0.5 < p_T < 3.0\,{\rm GeV}/c$), photon candidates are analyzed from different events (which necessarily removes all real combinations) to form a mixed event distribution. The mixed event pair distribution is normalized (green closed circles in Fig. 3) to the real pair distribution by taking the ratio of the real and mixed distributions and fitting with a constant at high invariant mass, and then subsequently scaling the mixed event distribution by this constant. The subtraction from this real pair distribution results in a final $\gamma\gamma$ invariant mass spectrum which has all uncorrelated background pairs removed (blue closed circles in Fig. 3). Using the same mixed event procedure, only a small fraction of the 4×4B background was found to be uncorrelated, the rest is made from a jet correlated background made primarily from π^0 decays. The mixed-event subtraction removes only a small fraction of the uncorrelated background in the 4×4B triggered dataset, so it is not applied in this case (see panels (c) and (d) in Fig. 3).

Raw yields are extracted by fitting the invariant mass distributions (mixed-event subtracted in minimum bias sample) with a function for the correlated background plus a constant term times a normalized Gaussian distribution representing the signal peak (gray lines in Fig. 3). The optimal background function for the minimum bias (4×4B) dataset was an exponential (Gamma Distribution) function. Variation of the functional form of the background (2nd, 3rd order polynomial) was used to evaluate the systematic uncertainty on the yield extrac-

tion.

C. Efficiency Corrections ($\epsilon_{\rm reco}$ and $\epsilon_{\rm trig}$)

Measured (raw) yields must be corrected for reconstruction and trigger inefficiencies. Simulations are used to calculate the reconstruction efficiency ($\epsilon_{\rm reco}$), which corrects for geometric acceptance and detector resolution effects. To produce an η meson p_T spectrum which is similar to that in real data, a full Monte Carlo sample of single η mesons are initially generated flat in p_T and pseudorapidity in the MPC kinematics, and with the same z-vertex distribution as measured in data. These generated single η mesons are passed through a GEANT (3.21) [54] description of the PHENIX detector and subsequent energy deposits are embedded into real data minimum bias events. Minimum bias events here do not necessarily contain an η meson from the collision. The same cluster identification and pair cuts are applied, followed by the full reconstruction, similar to that in the real data analysis.

The next step weights the reconstructed and generated η mesons in p_T and pseudorapidity to mimic the measured data distribution. This accounts for p_T smearing effects on an exponential spectrum, and for the falling pseudorapidity dependence in the forward region. As the weighting is dependent on the shape of the corrected spectrum, an iterative procedure is used to ensure the efficiency correction converges to a stable value. The reconstruction efficiency is calculated as the ratio of reconstructed η mesons divided by the number generated. The reconstruction efficiency for the South and North MPC for both triggers is shown in Fig. 4. The North MPC has a lower reconstruction efficiency than the South, due to a more restrictive noisy/inactive tower map in the North. The reconstruction efficiency shape is predominantly due to the geometric acceptance coupled to the narrowing $\gamma\gamma$ opening angle from low to higher momenta. At low momenta, wider opening angles can prohibit the measurement of both γs in the detector. At high momenta, cluster merging increasingly inhibits the detection of distinct γ pairs. Significant cluster merging effects occur when the cluster separation is less than 1.5 times the tower width ($\Delta R < 3.3$ cm).

The trigger efficiency ($\epsilon_{\rm trig}$) is estimated by taking the ratio of η meson yields found using the trigger of interest (for example minimum bias) in coincidence with any other trigger which is unrelated (unbiased) divided by the same unrelated trigger without the coincidence requirement,

$$\epsilon^{\eta}_{\rm trig} = \frac{N^{\eta}_{\rm unbias\wedge trig}}{N^{\eta}_{\rm unbias}} \qquad (3)$$

For the minimum bias trigger efficiency, $\epsilon^{\eta}_{\rm MB}$, the 4×4B trigger is used as this maximizes the η meson yield statistics. The measured minimum bias trigger efficiency is

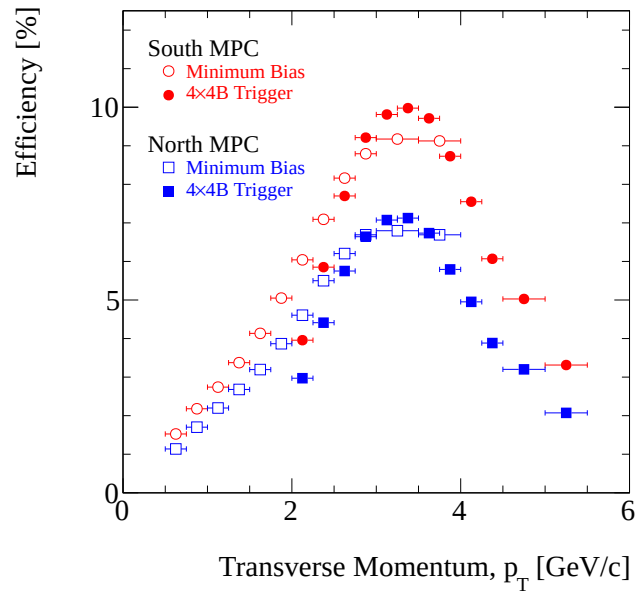

FIG. 4: (Color online) Reconstruction efficiency for η-mesons using the minimum bias (4×4B) dataset, shown as open (closed) symbols. The red/circle (blue/square) symbols show the η-meson reconstruction efficiency for the South (North) MPC.

found to be $\epsilon^{\eta}_{\rm MB} = 0.76 \pm 0.01\,({\rm stat}) \pm 0.06\,({\rm syst})$. There is a slight dependence on p_T, which has been factored into the systematic uncertainty.

For the 4×4B trigger efficiency for η mesons, $\epsilon^{\eta}_{4\times4{\rm B}}$, the minimum bias trigger is used as the unrelated trigger. The statistics in the minimum bias sample is limited, however, and the efficiency can only be determined from the data up to $p_T < 3.0$ GeV/c (see panel (c) in Fig. 5, open symbols). Instead, the trigger efficiency for η mesons in the 4×4B triggered sample is calculated by simulating the 4×4B trigger.

The 4×4B trigger comprises a total of 56 (61) overlapping 4×4 tower array sums from the South (North) MPC. An example of the efficiency of an individual 4×4 array from data is shown in panel (a) in Fig. 5. This efficiency is fit with a double error function

$$f(x) = \int_{-\infty}^{x} [a g_1(x') + (1-a) g_2(x')] dx' \qquad (4)$$

where $g_1(x)$ and $g_2(x)$ are Gaussian distributions. The efficiency curve shown in panel (a) of Fig. 5 covers the entire data-taking period, and relative gain changes throughout the RHIC run due to temperature variations and radiation damage to the detector cause a large spread in the rise of the efficiency curve. This gain variation is monitored with an LED calibration system. The trigger threshold ($\theta_{\rm thresh}$) at any given instant is a step function, and is thus implemented in the simulation as a step-function. The changes in the effective threshold due to

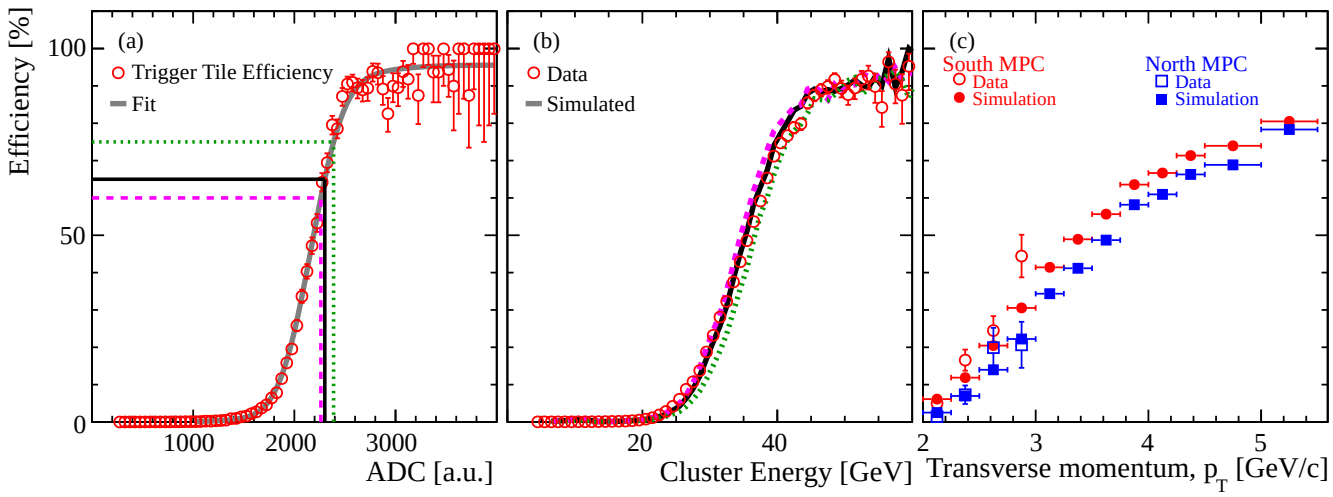

FIG. 5: (Color online) Panel (a) shows the trigger efficiency for a single 4×4 tower array in the 4×4B trigger. The solid, dashed, and dotted lines represent $\theta_{\rm thresh} = 0.66, 0.60,$ and 0.75, respectively. Panel (b) shows a comparison of the cluster efficiency as a function of energy to the simulated efficiency generated using the different θ_{thresh}. Panel (c) shows the η meson 4×4B trigger efficiency, $\epsilon^{\eta}_{4\times4\rm B}$ (systematic error not included). The open symbols represent $\epsilon^{\eta}_{4\times4\rm B}$ calculated using Eq. 3 with the minimum bias trigger as the unrelated trigger. The closed points represent $\epsilon^{\eta}_{4\times4\rm B}$ calculated from simulation. South (North) efficiencies are shown as circles (squares).

the gain variation over the run are accounted for in the simulation by varying the threshold using the data from the LED monitoring. Fit parameters from the 117 different trigger tile efficiency curves are derived and used in the trigger simulation to determine an optimal $\theta_{\rm thresh}$, and thus trigger efficiency for η mesons.

To tune the trigger simulation, reconstructed p+p events from PYTHIA (tune-A) [55] were processed through the trigger simulation and matched to real data. The cluster trigger efficiency is well reproduced in the simulation when using a mean tile trigger threshold of $\theta_{\rm thresh} = 0.66$, determined from the fit parameters in Eq. 4 (see solid line in panels (a) and (b)). On average, $\theta_{\rm thresh}$ corresponds to $\langle E_{4\times4}\rangle \approx 40$ GeV. The comparison is shown in panel (b) of Fig. 5, where good agreement is seen between the simulation of the 4×4B trigger and the data efficiency curve to all energies of interest in this analysis. Variations of the threshold in the simulation between $0.60 < \theta_{\rm thresh} < 0.75$ (see dotted (0.60) and dashed (0.75) lines in panels (a) and (b)) are used to estimate a systematic uncertainty on reproducing the 4×4B cluster trigger efficiency. These systematic variations account for differences in the South and North MPC, and for a turn-on uncertainty which occurs for low energy clusters that are smeared out above and below the selected trigger turn-on.

Within this trigger simulation framework, the 4×4B trigger efficiency for η mesons is calculated from the same single-η simulations used in the reconstruction efficiency study. This simulation accounts for effects such as when the distance between the two decay photons, ΔR, is small enough that the two photons fall into the same 4×4 tile such that their energy sum fires the trigger together. Panel (c) in Fig. 5 shows the η meson 4×4B trigger efficiency calculated via simulation, with a comparison to the statistically limited values measured from the minimum bias trigger in the overlap region of $2.0 < p_T < 3.0$ GeV/c calculated using Eq. 3. In this overlap region there is good agreement within statistical (shown) and systematic uncertainties (not shown, see next section).

D. Systematic Uncertainties

The systematic uncertainties are divided into three types. Statistical and point-to-point uncorrelated systematic uncertainties are added in quadrature to form type-A uncertainties. Type-B represent correlated uncertainties between p_T bins. Type-C are external global systematic uncertainties which underlay the measurement.

The functional form of the background used in the yield extraction was varied and contributes 5-15% to the type-A uncertainties. The systematic uncertainty due to energy scale (type-B) was found to vary from 3 to 30% for $p_T = 0.5$ to 5.0 GeV/c. A global reconstruction efficiency uncertainty (type-B) of 11.5 % (27.5%) is applied for $p_T > 0.75$ GeV/c ($p_T < 0.75$ GeV/c). An additional reconstruction efficiency uncertainty of 1 to 20% for $p_T = 3.0$ to 5.0 GeV/c is assigned due to cluster merging effects (type-B). The systematic uncertainty on varying the turn-on threshold (type-B) for the 4×4B trigger efficiency leads to 30% uncertainty at $p_T = 2.0$ GeV/c, which decreases exponentially to 5% at $p_T = 5.0$ GeV/c. A further global (type-C) systematic uncertainty of 9.7 % is applied based on the luminosity monitoring of the

BBC.

E. Cross Section Results

The cross section is calculated using Eq. 2 independently for the South and North MPC, and for both the minimum bias and 4×4B data sets. For both trigger conditions, the South and North reconstructed cross section agree to within 2% across p_T. The South and North cross section measured for each trigger are weighted together to determine the final cross section spectrum. Agreement in the overlap region ($2 < p_T < 3\,\mathrm{GeV}/c$) between the minimum bias and 4×4B cross section was within 7% across p_T and are within the type-A systematic uncertainties. In the overlapping region, data points from the two data sets are combined as a weighted average.

The invariant cross section of η mesons is shown in Figure 6 and Table I as a function of transverse momentum, measured between $0.5 < p_T < 5.0$ GeV/c within a pseudorapidity range of $3.0 < |\eta| < 3.8$. The results are compared to a NLO pQCD calculation [56, 57], over the same pseudorapidity region as the measurement. The lower panel shows the comparison between the measured cross section and the NLO pQCD. For $p_T > 2.0\,\mathrm{GeV}/c$, the NLO pQCD calculation is in very good agreement with the measured cross section. Upon approaching the pQCD limit at low momentum ($p_T < 2.0\,\mathrm{GeV}/c$) the agreement is less clear, but well within the factorization uncertainty.

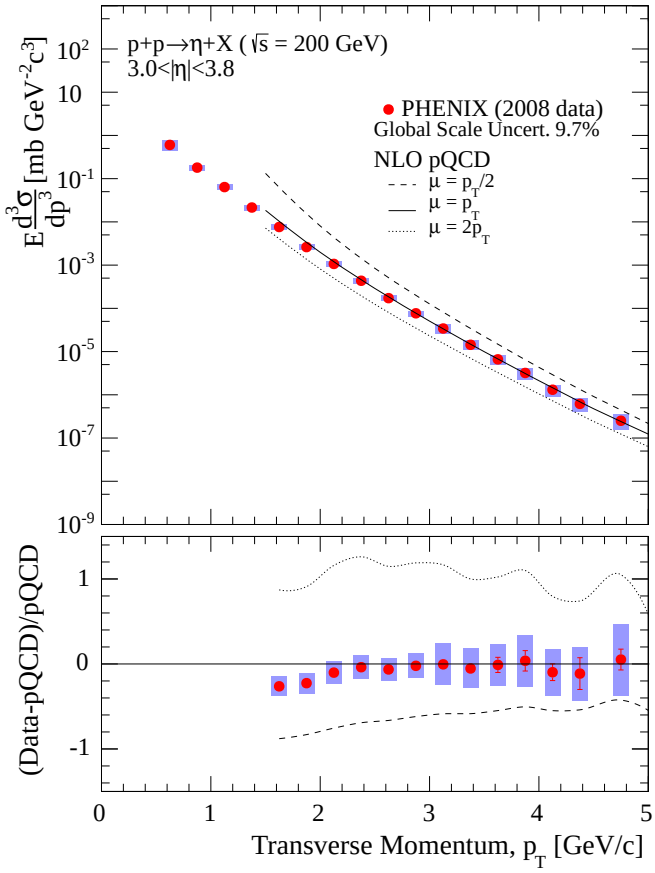

FIG. 6: (Color online) The cross section of inclusive η mesons produced from p+p collisions at $\sqrt{s} = 200$ GeV at forward rapidity. The upper panel shows the measured cross section versus transverse momentum (p_T), compared to an NLO pQCD calculation [56, 57]. The lower panel shows the difference between the measured cross section and each of the NLO pQCD calculations. Error bars (bands) represent type-A (type-B) systematic uncertainties. A global scale uncertainty (type-C, 9.7%) is due to the luminosity and global reconstruction uncertainties.

V. THE TRANSVERSE SINGLE SPIN ASYMMETRY FOR η MESONS

In polarized $p^{\uparrow}$+p collisions, the cross section of hadron production can be modified in azimuth, with respect to the polarization direction. To first order the azimuthally dependent cross section can be written as

$$\frac{\mathrm{d}\sigma}{\mathrm{d}\Omega} = \left(\frac{\mathrm{d}\sigma}{\mathrm{d}\Omega}\right)_0 (1 + P_y \cdot A_N \cdot \cos\phi) \tag{5}$$

where $\left(\frac{\mathrm{d}\sigma}{\mathrm{d}\Omega}\right)_0$ is the unpolarized differential cross section, P_y is the vertical beam polarization, and A_N is the transverse single spin asymmetry. This dependence can be measured as

$$P_y \cdot A_N \cdot \cos\phi = \epsilon_N(\phi) \tag{6}$$

where $\epsilon_N(\phi)$ is the measured raw asymmetry which, to first order, is an azimuthal cosine modulation. For this analysis, A_N is found by first measuring the raw asymmetry ($\epsilon_N(\phi)$), fitting it with a cosine function, and then dividing the amplitude by the average beam polarization. The raw asymmetry is measured in this analysis using two methods [58].

The first method is known as the polarization formula,

$$\epsilon_N^{\mathrm{pol}}(\phi) = \frac{N^{\uparrow}(\phi) - N^{\downarrow}(\phi)}{N^{\uparrow}(\phi) + N^{\downarrow}(\phi)} \tag{7}$$

which uses two different polarization yields (up - ↑ and down - ↓) in one azimuthal region. This method is preferred if the acceptance is not homogeneous, but relative luminosity effects ($\mathcal{R} = \frac{\mathcal{L}^{\uparrow}}{\mathcal{L}^{\downarrow}}$) must be taken into account.

A second method is known as the square-root formula, Eq. 8, which uses the geometric mean of the yields N from two azimuthal regions on opposite sides of the MPC (ϕ and ϕ+π) and two polarization directions (up – ↑ and down – ↓). When there is little loss of acceptance, particularly dead areas in azimuthal space, this method is advantageous as detector efficiency and relative luminosity effects cancel.

TABLE I: The measured η meson cross section versus p_T at forward rapidity for the 2008 dataset with statistical and systematic (type-A and type-B) uncertainties. There is an additional normalization uncertainty of 9.7% (type-C).

p_T	$E\frac{d^3\sigma}{dp^3}$ [mb GeV$^{-2}c^3$]		
[GeV/c]	Yield	Type-A	Type-B
0.625	6.03e+02	8.76e+01	1.68e+02
0.875	1.80e+02	3.12e+01	2.61e+01
1.125	6.39e+01	4.48e+00	9.71e+00
1.375	2.15e+01	8.17e-01	3.35e+00
1.625	7.61e+00	3.98e-01	1.17e+00
1.875	2.61e+00	1.31e-01	4.08e-01
2.125	1.07e+00	5.31e-02	1.59e-01
2.375	4.35e-01	2.04e-02	6.33e-02
2.625	1.72e-01	6.39e-03	2.39e-02
2.875	7.68e-02	3.08e-03	1.13e-02
3.125	3.42e-02	1.19e-03	8.42e-03
3.375	1.43e-02	8.87e-04	3.53e-03
3.625	6.61e-03	5.96e-04	1.62e-03
3.875	3.20e-03	3.71e-04	9.41e-04
4.125	1.31e-03	1.42e-04	3.95e-04
4.375	6.17e-04	1.30e-04	2.17e-04
4.750	2.51e-04	2.92e-05	1.01e-04
5.250	1.55e-05	1.37e-05	8.04e-06

$$\epsilon_N^{\sqrt{\phi}} = \frac{\sqrt{N^{\uparrow}(\phi)\cdot N^{\downarrow}(\phi+\pi)} - \sqrt{N^{\downarrow}(\phi)\cdot N^{\uparrow}(\phi+\pi)}}{\sqrt{N^{\uparrow}(\phi)\cdot N^{\downarrow}(\phi+\pi)} + \sqrt{N^{\downarrow}(\phi)\cdot N^{\uparrow}(\phi+\pi)}} \tag{8}$$

The final transverse single spin asymmetry result reported uses the square-root formula. The polarization formula serves as a cross check.

A. Polarization

To measure A_N, the polarization and spin information of only one beam is used, while the other beam's spin information is ignored, such that it is integrated over to a net polarization of zero. As one chooses which beam to use as 'polarized', two independent A_N measurements can be made: one utilizing the North-going beam's polarization, and one utilizing the South-going beam's polarization. Effectively, as the South and North MPC detectors are independent with differing systematics, two independent measures of A_N are derived, allowing for more reliable evaluation of systematic uncertainties on the results.

B. A_N Analysis

To measure the raw A_N, the ϕ distribution of the reconstructed η-meson is divided into twelve azimuthal bins, and spin dependent η meson yields are obtained for each bin.

To extract the η meson yields for the A_N measurements, the invariant mass spectra from all photon pairs are first formed independent of spin direction and ϕ, binned in x_F (or p_T). These invariant mass spectra are then fit with a signal Gaussian and background function. The signal Gaussian establishes the peak mass (M_η) and width (σ_η) which are used to define an η mass window for the given x_F (p_T) bin. The counts from the background function and signal are also used to form a relative contribution under the peak region from the background ($r = \frac{N_{\rm BG}}{N_{\rm BG}+N_\eta}$).

Spin dependent and ϕ dependent invariant mass spectra are then formed, with the spin and ϕ dependent yields determined by integrating the invariant mass spectra between $M_\eta \pm 2\sigma_\eta$. An example of the signal and background regions are shown in Fig. 7.

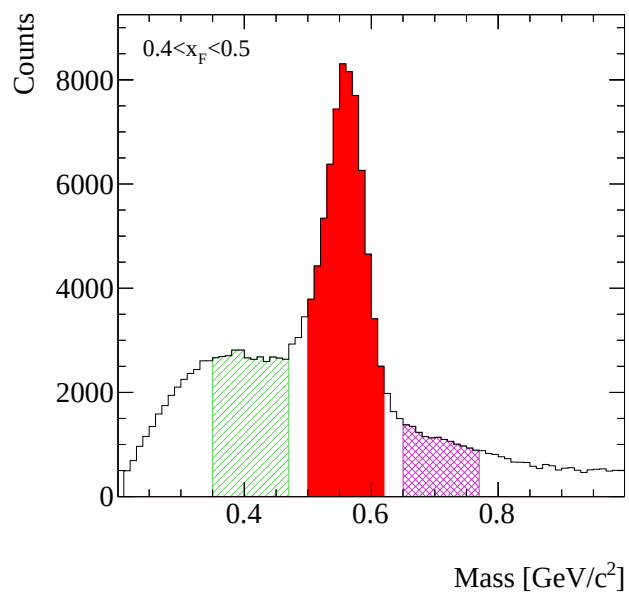

FIG. 7: (Color online) Invariant mass spectrum for the South MPC, illustrating the η meson peak region (solid fill), as well as the side band regions (diagonal fill and cross-hatch).

The asymmetry in the peak region, $\epsilon_N^{M\pm 2\sigma}$ is then simply calculated from Eqs. 7 and 8. The resultant asymmetries are then fit with a cosine function, see Fig. 8.

The transverse single spin asymmetry in the η meson peak region is then calculated, $A_N^{M\pm 2\sigma}$, using Eq. 6. As mentioned, the amplitude of the cosine function, divided by the beam polarization gives the value of $A_N^{M\pm 2\sigma}$. Because a significant background remains under the η mass region, the final measurement of A_N must be corrected for any dilution of the asymmetry due to this background.

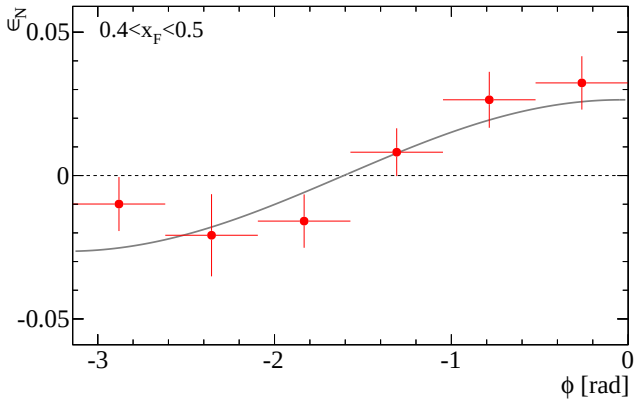

FIG. 8: (Color online) An example of a raw (square root method) asymmetry fit for a single x_F bin in the South MPC.

This background is comprised of non-η meson particles, which may have a different asymmetry than the signal η mesons. The correction is obtained from the asymmetry measured from a combined mass region from regions below ($M_{-5\sigma} < m_{inv} < M_{-3\sigma}$ GeV/c^2) and above ($M_{3\sigma} < m_{\rm inv} < M_{5\sigma}$ GeV/c^2) the η meson mass peak, shown as the diagonal and cross-hatch filled regions in Fig. 7, respectively. The background-corrected η meson asymmetry is expressed as:

$$A_N^{\eta} = \frac{A_N^{M\pm 2\sigma} - r A_N^{\rm bg}}{1-r} \tag{9}$$

where r is the background fraction in the $\pm 2\sigma$ region around the η mass peak, $A_N^{M\pm 2\sigma}$ is the measured asymmetry of the peak region, and $A_N^{\rm bg}$ is the measured asymmetry of the background regions. The r values are found from the spin-independent signal and background invariant mass spectrum fits mentioned above. For the lowest x_F bins, calculated from the minimum bias data, $\langle r_{\rm MB}\rangle = 0.60$. For the highest x_F bins, calculated from the 4×4B data, $\langle r_{4\times 4\rm B}\rangle = 0.37$. $A_N^{\rm bg}$ was found to be consistent in the low and high mass regions. Overall the background correction from Eq. 9 had a moderate effect of $A_N^{\eta} > A_N^{M\pm 2\sigma}$. A table summarizing $A_N^{M\pm 2\sigma}$ and $A_N^{\rm bg}$ from the 4×4B triggered dataset is given in Table II.

C. A_N Results

The x_F-dependent A_N is shown in Fig. 9 and Table III, based on the weighted mean of the measured South and North MPC A_N^{η} values. The average pseudorapidity of the measured η mesons is $\langle\eta\rangle = 3.52$. The procedure to obtain A_N from the minimum bias triggered dataset is the same as that in the 4×4B dataset, and where the triggers overlap in x_F, the A_N values are weighted together. For forward x_F ($x_F > 0$), a clear rising asymmetry is seen, ranging from 2% to 20% over the measured

TABLE II: $A_N^{M\pm 2\sigma}$ and $A_N^{\rm bg}$ for η mesons measured as a function of x_F from the 4×4B triggered dataset. The values represented are the weighted mean of the South and North MPC. The uncertainties listed are statistical only.

x_F bin	$A_N^{M\pm 2\sigma}$	Stat	$A_N^{\rm bg}$	Stat.
-0.7 to -0.6	-0.0385	0.0602	0.0366	0.1256
-0.6 to -0.5	0.0110	0.0186	-0.0484	0.0360
-0.5 to -0.4	0.0094	0.0094	-0.0261	0.0178
-0.4 to -0.3	0.0135	0.0117	0.0186	0.0199
0.3 to 0.4	0.0314	0.0127	0.0028	0.0208
0.4 to 0.5	0.0537	0.0102	0.0242	0.0190
0.5 to 0.6	0.0353	0.0196	0.0458	0.0380
0.6 to 0.7	0.0974	0.0628	0.0147	0.131

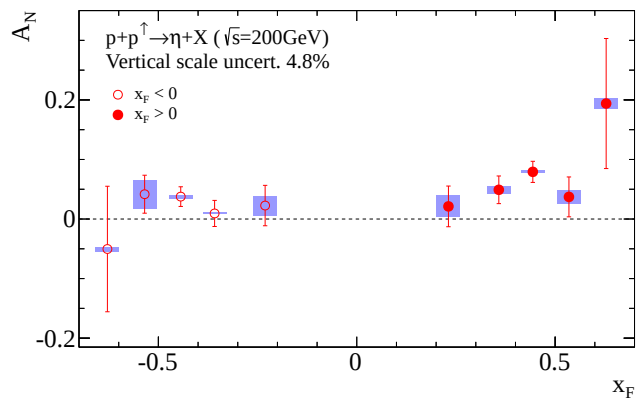

FIG. 9: (Color online) The x_F dependence of A_N. The vertical error bars show the statistical uncertainty, the blue bands represent uncorrelated systematic uncertainties (see text for details). The relative luminosity effect systematic uncertainties are not shown (see text and Table III)

x_F range. For backward x_F ($x_F < 0$), A_N is flat and consistent with zero when averaged over x_F within 1.7σ of the statistical plus systematic uncertainties. An uncorrelated systematic uncertainty is shown as bands around the points, and is found by varying the functional form of the background functions. This changes the $M \pm 2\sigma$ range and relative r values, which affects the number of η mesons used in the calculation of A_N. It also includes systematic uncertainty estimation from three different cross checks on the measurement of A_N: increasing the mass window to $M \pm 2.5\sigma$, the difference from the polarization formula measurement (Eq. 7), and adding higher order cosine terms to the raw asymmetry fit. The correlated systematic uncertainty (not shown on Fig. 9, see Table III) is due to small residual relative luminosity effects in the square root formula.

Figure 10 shows the measured A_N for η mesons com-

TABLE III: A_N for η mesons measured as a function of x_F. Uncertainties listed are those due to the statistics, the x_F uncorrelated uncertainties due to extracting the yields, and the correlated relative luminosity uncertainty (see text for details).

x_F bin	$\langle x_F \rangle$	$\langle p_T \rangle$ [GeV/c]	A_N^η	Uncertainty stat	uncorr	corr
-0.7 to -0.6	-0.63	3.41	-0.0503	0.1054	0.0791	0.0024
-0.6 to -0.5	-0.535	3.04	0.0417	0.0319	0.0385	0.0023
-0.5 to -0.4	-0.444	2.68	0.0376	0.0165	0.0161	0.0021
-0.4 to -0.3	-0.358	2.34	0.0094	0.0219	0.0095	0.0023
-0.3 to -0.2	-0.231	1.35	0.0226	0.0339	0.0179	0.0000
0.2 to 0.3	0.231	1.35	0.0212	0.0342	0.0204	0.0000
0.3 to 0.4	0.358	2.34	0.0491	0.0232	0.0127	0.0020
0.4 to 0.5	0.444	2.68	0.0792	0.0177	0.0083	0.0018
0.5 to 0.6	0.535	3.04	0.0372	0.0335	0.0179	0.0020
0.6 to 0.7	0.629	3.41	0.1939	0.1092	0.0392	0.0019

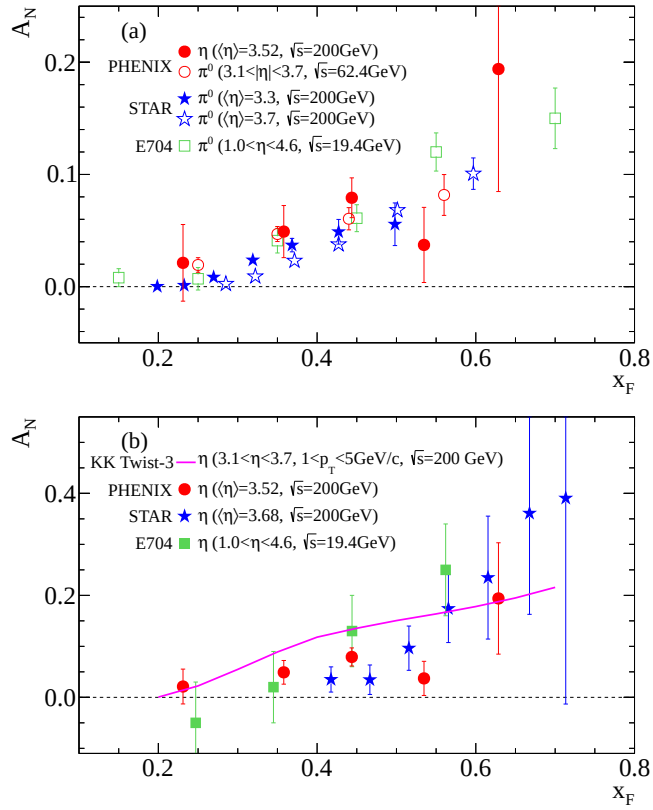

FIG. 10: (Color online) Comparison between the η meson A_N and other results. Panel (a) compares with π^0 meson A_N results from PHENIX [15], STAR [13], and E704 [9] in red/circle, blue/star, and green/square symbols, respectively. Panel (b) compares to the STAR η meson A_N result [14] (blue stars), the E704 η meson A_N result [11] (green squares) and a twist-3 calculation [59] (curve).

pared to other A_N measurements. The upper panel shows a comparison between η meson and π^0 meson asymmetries in overlapping x_F and similar pseudorapidity ranges at various collision energies. The η meson A_N is similar to the π^0 A_N measurements at a lower center-of-mass energy made by the PHENIX experiment using the MPC [15], as well as π^0 from the E704 [9] and STAR [13] experiments. The similarity between the η and π^0 asymmetries suggests that initial-state spin-momentum correlations could play a role, or a common spin-momentum correlation is present in the fragmentation of π^0 and η mesons.

The lower panel of Fig. 10 shows a comparison to measurements made by E704 [11] ($\sqrt{s} = 19.4$ GeV) and STAR [14] at the same collision energy ($\sqrt{s} = 200$ GeV). The average pseudorapidity of the PHENIX result is $\langle \eta \rangle = 3.52$, while the average pseudorapidity of the STAR result is $\langle \eta \rangle = 3.68$. For $x_F > 0.55$, the STAR η meson A_N is larger than this PHENIX η meson A_N measurement, but these two results are consistent with each other within type-A uncertainties.

The asymmetries in Fig. 10 are compared to a twist-3 calculation by Kanazawa and Koike [59] based on [40], performed for the PHENIX kinematics. It describes the magnitude of the asymmetry well at the lowest and highest points in x_F, but it is unclear whether the observed shape for the middle x_F values is well described. No theoretical uncertainty on the calculation is available at this time; a better understanding of the theoretical uncertainties will be necessary in order to draw a quantitative conclusion on the agreement with data.

The p_T dependence of the asymmetry is shown in Fig. 11 and Table IV. For A_N measured at forward x_F ($x_F > 0.2$), a clear nonzero asymmetry is seen ($\langle A_N \rangle = 0.061 \pm 0.012$), while A_N for backward x_F ($x_F < -0.2$) is consistent with zero within 1.7σ. The uncorrelated and correlated systematic uncertainties are evaluated the same way as in the x_F dependence of A_N.

Figure 11 also shows the measured A_N as a function of p_T compared to the twist-3 calculations. Similar to the case for the x_F dependence, the twist-3 calculation describes the magnitude of the asymmetry well at the lowest and highest measured points in p_T, but it is not clear if it describes the observed shape in the mid-p_T range. It should be noted that the data points in p_T are integrated over a wide range of x_F, $0.2 < x_F < 0.7$.

VI. SUMMARY

By utilizing data taken by the MPC detector installed at forward rapidity in the PHENIX experiment at RHIC, the invariant cross section as a function of p_T and the transverse single spin asymmetry A_N as a function of x_F and p_T have been measured for inclusive η mesons produced at forward rapidity ($\langle \eta \rangle = 3.52$) from $p^\uparrow + p$

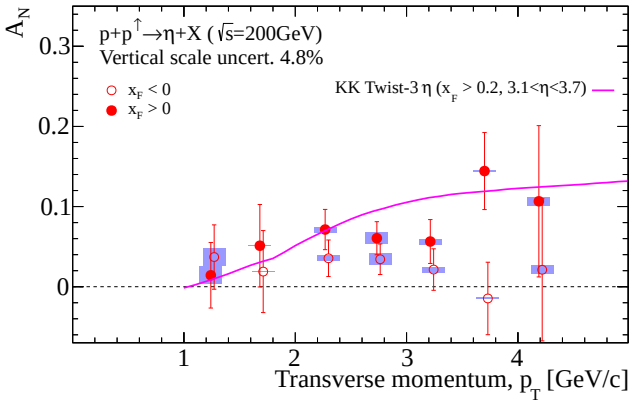

FIG. 11: (Color online) The p_T dependence of A_N. The vertical error bars show the statistical uncertainty; the blue bands represent uncorrelated systematic uncertainties (see text for details). The relative luminosity effect systematic uncertainties are not shown (see text and Table IV). The purple line shows a prediction from a twist-3 calculation based on quark-gluon correlation functions [59].

collisions at a center-of-mass energy of $\sqrt{s} = 200$ GeV. The NLO pQCD calculation was found to be consistent with the invariant cross section measurement at momentum of $p_T > 1.5$ GeV/c. This measurement can be used to improve constraints on the hadronization process of η mesons in future global analyses of the η fragmentation function. Non-zero asymmetries measured at forward x_F are consistent with previous π^0 meson results within statistical uncertainties. Because the π^0 and η mesons are produced from potentially different parton fractions, and also might have different polarized fragmentation functions due to isospin or mass differences or the presence of strange quarks in the η, this data will help to constrain the relative importance of spin-momentum correlations in the initial state polarized protons versus that of spin-momentum correlations in the fragmentation. The dependencies of the measured asymmetry on x_F and p_T are reasonably well described by twist-3 calculations using quark-gluon correlation functions; a quantitative comparison can be made once uncertainties become available on the calculations. With higher statistics from future data sets, a doubly differential measurement of the asymmetry binned in both x_F and p_T simultaneously could provide a much more stringent test of any available calculations and better constrain twist-3 quark-gluon correlation functions if they turn out to be the dominant contribution.

ACKNOWLEDGMENTS

We thank the staff of the Collider-Accelerator and Physics Departments at Brookhaven National Laboratory and the staff of the other PHENIX participating institutions for their vital contributions. We acknowledge support from the Office of Nuclear Physics in the Office of Science of the Department of Energy, the National Science Foundation, Abilene Christian University Research Council, Research Foundation of SUNY, and Dean of the College of Arts and Sciences, Vanderbilt University (U.S.A), Ministry of Education, Culture, Sports, Science, and Technology and the Japan Society for the Promotion of Science (Japan), Conselho Nacional de Desenvolvimento Científico e Tecnológico and Fundação de Amparo à Pesquisa do Estado de São Paulo (Brazil), Natural Science Foundation of China (P. R. China), Ministry of Science, Education, and Sports (Croatia), Ministry of Education, Youth and Sports (Czech Republic), Centre National de la Recherche Scientifique, Commissariat à l'Énergie Atomique, and Institut National de Physique Nucléaire et de Physique des Particules (France), Bundesministerium für Bildung und Forschung, Deutscher Akademischer Austausch Dienst, and Alexander von Humboldt Stiftung (Germany), OTKA NK 101 428 grant and the Ch. Simonyi Fund (Hungary), Department of Atomic Energy and Department of Science and Technology (India), Israel Science Foundation (Israel), National Research Foundation of Korea of the Ministry of Science, ICT, and Future Planning (Korea), Physics Department, Lahore University of Management Sciences (Pakistan), Ministry of Education and Science, Russian Academy of Sciences, Federal Agency of Atomic Energy

TABLE IV: A_N for η mesons measured as a function of p_T. Uncertainties listed are those due to the statistics, the p_T uncorrelated uncertainties due to extracting A_N, and the correlated relative luminosity uncertainty (see text for details).

p_T bin [GeV/c]	$\langle p_T \rangle$ [GeV/c]	$\langle x_F \rangle$	A_N^η	Uncertainty stat	uncorr	corr
		x_F < -0.2				
1.0 to 1.5	1.24	0.23	0.0370	0.0401	0.0117	0.0000
1.5 to 2.0	1.68	0.27	0.0189	0.0512	0.0233	0.0000
2.0 to 2.5	2.27	0.42	0.0355	0.0228	0.0183	0.0042
2.5 to 3.0	2.73	0.44	0.0343	0.0191	0.0136	0.0041
3.0 to 3.5	3.21	0.46	0.0214	0.0259	0.0149	0.0047
3.5 to 4.0	3.70	0.48	-0.0147	0.0452	0.0213	0.0053
4.0 to 4.5	4.19	0.51	0.0211	0.0887	0.0822	0.0057
		x_F > 0.2				
1.0 to 1.5	1.24	0.23	0.0143	0.0409	0.0131	0.0000
1.5 to 2.0	1.68	0.27	0.0511	0.0514	0.0120	0.0000
2.0 to 2.5	2.27	0.42	0.0713	0.0251	0.0176	0.0042
2.5 to 3.0	2.73	0.44	0.0605	0.0206	0.0085	0.0041
3.0 to 3.5	3.21	0.46	0.0564	0.0274	0.0078	0.0047
3.5 to 4.0	3.70	0.48	0.1443	0.0480	0.0306	0.0053
4.0 to 4.5	4.19	0.51	0.1066	0.0944	0.0257	0.0057

(Russia), VR and Wallenberg Foundation (Sweden), the U.S. Civilian Research and Development Foundation for the Independent States of the Former Soviet Union, the Hungarian American Enterprise Scholarship Fund, and the US-Israel Binational Science Foundation.

[1] I. Estermann, R. Frisch, and O. Stern, Nature **132**, 169 (1933).
[2] R. P. Feynman, Phys. Rev. Lett. **23**, 1415 (1969).
[3] J. D. Bjorken, Phys. Rev. **179**, 1547 (1969).
[4] J. D. Bjorken and E. A. Paschos, Phys. Rev. **185**, 1975 (1969).
[5] G. L. Kane, J. Pumplin, and W. Repko, Phys. Rev. Lett. **41**, 1689 (1978).
[6] W. H. Dragoset, J. B. Roberts, J. E. Bowers, H. W. Courant, H. Kagan, M. L. Marshak, E. A. Peterson, K. Ruddick, and R. D. Klem, Phys. Rev. D **18**, 3939 (1978).
[7] S. Saroff, B. R. Baller, G. C. Blazey, H. Courant, K. J. Heller, M. L. Marshak, M. A. Shupe, D. S. Barton, G. Bunce, A. S. Carroll, et al., Phys. Rev. Lett. **64**, 995 (1990).
[8] C. E. Allgower et al. (E925 Collaboration), Phys. Rev. D **65**, 092008 (2002).
[9] D. L. Adams et al. (E704 Collaboration)), Phys. Lett. **B264**, 462 (1991).
[10] D. L. Adams et al. (E704 Collaboration)), Phys. Lett. **B261**, 201 (1991).
[11] D. L. Adams et al. (E704 Collaboration)), Nucl. Phys. B **510**, 3 (1998).
[12] I. Arsene et al. (BRAHMS Collaboration), Phys. Rev. Lett. **101**, 042001 (2008).
[13] B. I. Abelev et al. (STAR Collaboration), Phys. Rev. Lett. **101**, 222001 (2008).
[14] L. Adamczyk et al. (STAR Collaboration), Phys. Rev. D **86**, 051101 (2012).
[15] A. Adare et al., (PHENIX Collaboration), arXiv:1312.1995.
[16] S. Heppelmann (STAR), PoS **DIS2013**, 240 (2013).
[17] S. Adler et al. (PHENIX Collaboration), Phys.Rev.Lett. **95**, 202001 (2005).
[18] D. Sivers, Phys. Rev. D **41**, 83 (1990).
[19] D. Sivers, Phys. Rev. D **43**, 261 (1991).
[20] A. Airapetian et al. (HERMES Collaboration), Phys. Rev. Lett. **94**, 012002 (2005).
[21] A. Airapetian et al. (HERMES Collaboration), Phys. Rev. Lett. **103**, 152002 (2009).
[22] M. Alekseev et al. (COMPASS Collaboration), Phys. Lett. B **692**, 240 (2010).
[23] C. Adolph et al. (COMPASS Collaboration), Phys. Lett. B **717**, 383 (2012).
[24] J. C. Collins, Nucl. Phys. B **396**, 161 (1993).
[25] K. Abe et al. (Belle Collaboration), Phys. Rev. Lett. **96**, 232002 (2006).
[26] R. Seidl et al. (Belle Collaboration), Phys. Rev. D **78**, 032011 (2008), ; Phys. Rev. D **86**, 039905 (2012).
[27] J. P. Lees et al., (BaBar Collaboration), arXiv:1309.5278.
[28] A. Airapetian et al. (HERMES Collaboration), Phys. Lett. B **693**, 11 (2010).
[29] C. Adolph et al. (COMPASS Collaboration), Phys. Lett. B **717**, 376 (2012).
[30] F. Yuan, Phys.Lett. **B666**, 44 (2008).
[31] M. Anselmino, M. Boglione, U. D'Alesio, E. Leader, S. Melis, et al., Phys.Rev. **D86**, 074032 (2012).
[32] M. Anselmino, M. Boglione, U. D'Alesio, S. Melis, F. Murgia, et al., Phys.Rev. **D88**, 054023 (2013).
[33] A. V. Efremov and O. V. Teryaev, Sov. J. Nucl. Phys. **36**, 140 (1982).
[34] A. V. Efremov and O. V. Teryaev, Phys. Lett. B **150**, 383 (1985).
[35] J.-w. Qiu and G. F. Sterman, Phys. Rev. Lett. **67**, 2264 (1991).
[36] J.-w. Qiu and G. F. Sterman, Phys. Rev. D **59**, 014004 (1999).
[37] Y. Kanazawa and Y. Koike, Phys. Lett. **B478**, 121 (1991).
[38] X. Ji, J.-W. Qiu, W. Vogelsang, and F. Yuan, Phys. Rev. Lett. **97**, 082002 (2006).
[39] K. Kanazawa and Y. Koike, Phys. Rev. D **82**, 034009 (2010).
[40] K. Kanazawa and Y. Koike, Phys. Rev. D **83**, 114024 (2011).
[41] A. Metz and D. Pitonyak, Phys.Lett. **B723**, 365 (2013).
[42] K. Kanazawa, Y. Koike, A. Metz, and D. Pitonyak, arXiv:1404.1033.
[43] T. C. Rogers and P. J. Mulders, Phys. Rev. D **81**, 094006 (2010).
[44] T. C. Rogers, Phys. Rev. D **88**, 014002 (2013).
[45] I. Alekseev et al., Nucl. Instrum. Methods Phys. Rev. Sec. A **499**, 392 (2003).
[46] K. Adcox et al., Nucl. Instrum. Methods Phys. Rev. Sec. A **499**, 469 (2003).
[47] I. Nakagawa et al., AIP Conf. Proc. **980**, 380 (2008).
[48] I. G. Alekseev et al., Phys. Rev. D **79**, 094014 (2009).
[49] Y. Fukao et al., Phys. Lett. B **650**, 325 (2007).
[50] A. Adare et al. (PHENIX Collaboration), Phys. Rev. D **88**, 032006 (2013).
[51] M. Ippolitov, S. Beloglovsky, S. Burachas, V. Ikonnikov, A. Kuryakin, et al., Nucl. Instrum. Methods Phys. Rev. Sec. A **537**, 353 (2005).
[52] J. Beringer et al. (Particle Data Group), Phys. Rev. D **86**, 010001 (2012).
[53] S. S. Adler et al. (PHENIX Collaboration), Phys. Rev. Lett. **91**, 241803 (2003).
[54] S. Agostinelli et al., Nucl. Instrum. Methods Phys. Rev. Sec. A **506**, 250 (2003).
[55] T. Sjostrand, S. Mrenna, and P. Skands, j. High Energy Phys. **05** (2006) 026.
[56] B. Jäger, A. Schäfer, M. Stratmann, and W. Vogelsang, Phys. Rev. D **67**, 054005 (2003).
[57] C. A. Aidala, F. Ellinghaus, R. Sassot, J. P. Seele, and M. Stratmann, Phys. Rev. D **83**, 034002 (2011).
[58] G. G. Ohlsen and P. W. Keatorn Jr., Nucl. Instrum. Meth. **109**, 41 (1973).
[59] K. Kanazawa and Y. Koike (2011), private communication. Calculation based on [40].